processes

MDPI

Article

Fabrication of Ultrathin MoS_2 Nanosheets and Application on Adsorption of Organic Pollutants and Heavy Metals

Siyi Huang [1], Ziyun You [1], Yanting Jiang [1], Fuxiang Zhang [1], Kaiyang Liu [1], Yifan Liu [1], Xiaochen Chen [1] and Yuancai Lv [1,2,*]

[1] Fujian Provincial Engineering Research Center of Rural Waste Recycling Technology, College of Environment & Resources, Fuzhou University, Fuzhou 350116, China; N170620033@fzu.edu.cn (S.H.); 061700527@fzu.deu.cn (Z.Y.); 061700506@fzu.deu.cn (Y.J.); 061700529@fzu.deu.cn (F.Z.); liukaiyang123@hotmail.com (K.L.); yfanym@fzu.edu.cn (Y.L.); chenxiaochen@fzu.edu.cn (X.C.)

[2] Research Institute of Photocatalysis, Fuzhou University, Fuzhou 350116, China

* Correspondence: yclv@fzu.edu.cn; Tel.: +86-135-6003-1596

Received: 10 April 2020; Accepted: 24 April 2020; Published: 26 April 2020

Abstract: Owing to their peculiar structural characteristics and potential applications in various fields, the ultrathin MoS_2 nanosheets, a typical two-dimensional material, have attracted numerous attentions. In this paper, a hybrid strategy with combination of quenching process and liquid-based exfoliation was employed to fabricate the ultrathin MoS_2 nanosheets (MoS_2 NS). The obtained MoS_2 NS still maintained hexagonal phase (2H-MoS_2) and exhibited evident thin layer-structure (1–2 layers) with inconspicuous wrinkle. Besides, the MoS_2 NS dispersion showed excellent stability (over 60 days) and high concentration (0.65 ± 0.04 mg mL^{-1}). The MoS_2 NS dispersion also displayed evident optical properties, with two characteristic peaks at 615 and 670 nm, and could be quantitatively analyzed with the absorbance at 615 nm in the range of 0.01–0.5 mg mL^{-1}. The adsorption experiments showed that the as-prepared MoS_2 NS also exhibited remarkable adsorption performance on the dyes (344.8 and 123.5 mg g^{-1} of q_m for methylene blue and methyl orange, respectively) and heavy metals (185.2, 169.5, and 70.4 mg g^{-1} of q_m for Cd^{2+}, Cu^{2+}, and Ag^{+}). During the adsorption, the main adsorption mechanisms involved the synergism of physical hole-filling effects and electrostatic interactions. This work provided an effective way for the large-scale fabrication of the two-dimensional nanosheets of transition metal dichalcogenides (TMDs) by liquid exfoliation.

Keywords: transition metal dichalcogenides; liquid exfoliation; adsorption; quenching

1. Introduction

Given the special structure and potential applications, two-dimensional materials have drawn plenty of concerns [1,2], such as graphene, boron nitride, and molybdenum disulfide. Among them, the ultrathin molybdenum disulfide (MoS_2) nanosheets, which exhibit an evident layered structure, have attracted ample attentions because of their excellent performance on several fields, such as catalysis, sensors, and pollution remediation [1,3]. Recently, the ultrathin MoS_2 nanosheets were reported to show excellent prospects in pollution control [3,4]. Therefore, it was urgent to explore an effective method to produce ultrathin MoS_2 nanosheets.

To date, a few methods have been reported for efficient preparation of ultrathin MoS_2 nanosheets [5–10], for example, mechanical exfoliation, sputtering, atomic layer deposition, chemical methods, and liquid-based exfoliation. In spite of the excellent performance of the prepared monolayer or few-layer MoS_2 nanosheets through mechanical methods, the production efficiency was rather low, which severely limited the large-scale applications. Meanwhile, although most of the chemical

methods like hydrothermal and solvent thermal routes could produce large-scale few-layer MoS_2 nanosheets, they generally needed strict reaction control, such as high temperature and pressure. Instead, due to the controllable operation and high production, liquid-based exfoliation was regarded as the most promising way for the production of ultrathin MoS_2 in large scale. According to previous studies [7,8], the solvent showed a significant impact on the exfoliation of MoS_2. Among which, pyrrolidone-based solvents like *N*-methyl-2-pyrrolidone displayed excellent MoS_2 exfoliation efficiency with 0.3 mg mL^{-1} of MoS_2 nanosheets concentration, because they showed similar surface energy with MoS_2. Nevertheless, considering their significant environmental risk, high toxicity and high-boiling points of the pyrrolidone-based solvents probably limited the large-scale application. To replace these toxic solvents, a number of polar solvents that own low boiling point and molecular weight were tested, such as water, methanol, ethanol, and isopropanol [11,12]. Unfortunately, given the different surface energy between the MoS_2 and polar solvents, most of the polar solvents showed dissatisfactory exfoliation efficiency [11]. Interestingly, it was reported that the MoS_2 exfoliation efficiency in the mixed solution with two of the polar micromolecular solvents was much better than those in the single solvent [13,14]. Meanwhile, it was worth noting that the MoS_2 exfoliation efficiency could be significantly improved when some organic small molecules, surfactants, or polymers were added in the polar micromolecular solvents, such as sodium cholate, Tween 80, Tween 85, sodium naphthalenide, Brij 30, Brij 700, Triton X-100, and so on [15–17]. Nevertheless, the strong van der Waals interaction between the MoS_2 layers still limited the MoS_2 nanosheets production.

Recently, owing to the effective break of the van der Waals force between the MoS_2 layers, quenching was found to be an effective way to exfoliate the graphene analogues [18–21]. Previous investigation showed that the high-quality ultrathin graphene sheets were fabricated by rapidly cooling the hot bulk graphite and pre-expanded graphite in aqueous solutions of NH_4HCO_3 and hydrazine hydrate, respectively [19,20]. Meanwhile, the boron nitride and MoS_2 nanosheets were also synthesized via the rapid quenching of hot bulk boron nitride and MoS_2 in the liquid N_2 [18,21]. Although the production efficiency of the nanosheets was dissatisfactory, we suspect that if the bulk MoS_2 was pretreated with the quenching process, the exfoliation efficiency of MoS_2 nanosheets in the polar micromolecular solvents could be significantly improved.

Herein, a hybrid strategy with the combination of quenching process and liquid-based exfoliation was employed to fabricate the ultrathin MoS_2 nanosheets. The microstructures, morphology, and optical properties were analyzed. In addition, the adsorption performance of dyes and heavy metals was also discussed.

2. Material and Methods

2.1. Materials

Ammonium tetrathiomolybdate ($(NH_4)_2MoS_4$) was provided by Sam Chemical Technology Co., Ltd. (Shanghai, China). Hydrazine monohydrate ($N_2H_4{\cdot}H_2O$) was provided by Aladdin Reagent Co., Ltd. (Shanghai, China). Sodium hydroxide (NaOH), sulfuric acid (H_2SO_4), nitric acid (HNO_3), methylene blue (MB), methyl orange (MO), $AgNO_3$, $CuSO_4$, and $CdCl_2$ were obtained from Sinopharm Chemical Reagent Co. Ltd. (Shanghai, China). The double-distilled water was prepared with a Milli-Q water purification system (Milli-Q®Reference, Millipore, Billerica, Massachusetts, USA).

2.2. Fabrication of the MoS_2 Nanosheets

The MoS_2 nanosheets (MoS_2-NS) were prepared through a novel combined method including calcination at high temperature, quenching with liquid nitrogen, and ultrasonic-assisted peeling with hydrazine hydrate. Firstly, 4.000 g of $(NH_4)_2MoS_4$ was calcinated under nitrogen atmosphere at 800 °C for 5 h with a rate of 5 °C/min and then a black powder (named bulk MoS_2) was obtained. After that, the high-temperature bulk MoS_2 was quickly transferred into a Dewar bottle containing liquid nitrogen until the liquid nitrogen gasified completely. Subsequently, the pre-expanded bulk

MoS_2 was transferred into a serum bottle with 100 mL of hydrazine hydrate and the bottle was sonicated at a frequency of 40 kHz for 24 h. After centrifugation, the residual MoS_2 powders were added into another serum bottle with deionized water and sonicated for 12 h (In addition, the recycled hydrazine hydrate can be reused in a new procedure.). Finally, the resulting suspensions were centrifuged at 3000 rpm for 2 h and then the dark green MoS_2-NS dispersions were obtained. After dialyzed with dialysis tubing with 3000 dalton of molecular weight cut off, the obtained ultimate green dispersions were close to 7 of pH and stored in the fridge at 4 °C.

2.3. Adsorption Batch Experiments

Adsorption isotherm batch experiments were carried out in a 40-mL serum bottle containing 10 mL liquid with 0.1 g L^{-1} of the adsorbent concentration. The adsorption isotherm for MB and MO was conducted under 25 °C in the range of 0.5 to 50 mg L^{-1} of the MB and MO concentration and the pH was adjusted to 6.0 ± 0.1 with 1 M H_2SO_4 solution, while the experiments for heavy metals were conducted under 25 °C with metal concentration from 0.5 to 30 mg L^{-1} and the pH was adjusted to 5.0 ± 0.1 with 1 M H_2SO_4 solution. After sealed with polytetrafluoroethylene (PTFE) caps, all the bottles were shaken at 250 rpm for 6 h. At sampling points, one bottle was taken out. After filtered with 0.22 μm glass fiber filters (Tianjin Branch billion Lung Experimental Equipment Co., Ltd., Tianjin, China), the MB/MO concentrations were determined by UV-vis spectroscopy (UV-1780, SHIMADZU, Japan) at 664/464 nm, while the residual Cu^{2+}/Cd^{2+}/Ag^{+} concentrations were analyzed with ICP-MS (XSERIES 2, Thermo). The adsorption isotherms data were treated with Langmuir and Freundlich models [22,23]. The experiments for the adsorption kinetics study were operated at 25 °C and 6.0 ± 0.1/5.0 ± 0.1 of pH (adjusted with 1 M H_2SO_4 solution) in 300 mL dyes/heavy metals solution (20 mg L^{-1} for dyes and 15 mg L^{-1} for heavy metals). All the samples were shaken at 250 rpm for 6 h. At sampling points, 1.5 mL of the solution was taken out and then filtered through the filters. The residual dyes/heavy metals concentrations were determined with ICP-MS. The adsorption kinetics data were treated with the pseudo-first order kinetic and pseudo-second-order non-linear kinetic models.

To study the effects of pH values (2–10)/(3–7) on dyes/heavy metals adsorption, the batch experiments were conducted at 25 °C in a serum bottle with 20 mg L^{-1}/15 mg L^{-1} of dyes/heavy metals concentration and 0.10 g L^{-1} of adsorbents.

2.4. Characterization

The X-ray powder diffraction (XRD) data of the bulk MoS_2 and MoS_2-NS were tested with X-ray powder diffractometer (MiniFlex600, Rigaku, Milwaukee, Wisconsin, USA) coupled with a Cu *Kα* line at 40 kV and 40 mA.

The microstructural features of prepared bulk MoS_2 and MoS_2-NS were observed with field emission scanning electron microscope (FESEM, Nova NanoSEM 230, FEI, Hillsboro, Oregon, USA), atomic force microscope (AFM, 5500, Agilent USA), and transmission electron microscope (TEM, TECNAI G2F20, FEI, Hillsboro, Oregon, USA).

The Raman data of bulk MoS_2 and MoS_2-NS were recorded by a confocal laser Raman microscopy (Invia Reflex, Renishaw, UK) with 532 nm of laser wavelength and 0.6 mW of laser energy.

The X-ray photoelectron spectroscopy (XPS) data were recorded with X-ray photoelectron spectrometer (ESCALAB 250, Thermo Scientific, Waltham, Massachusetts, USA) coupled with the Al *Ka* radiation at 15 kV and 51 W. The binding energies were confirmed by using the C1s component as the reference and the binding energy of C-C/H bonds were set at 284.5 eV.

The concentrations of MoS_2-NS dispersions were analyzed using UV-vis spectrophotometer (UV-2500, Shimadzu, Japan).

The Brunauer–Emmett–Teller (BET) surface areas of the bulk MoS_2 and MoS_2-NS were obtained from the analysis of N_2-adsorption isotherms at 77 K using the N_2 physisorption analyzer (ASAP2020, Micromeritics, Norcross, Georgia, USA).

3. Results and Discussion

3.1. Characterization of MoS_2 Nanosheets

3.1.1. Microstructures and Morphology

To study the variation of the crystal structure during the MoS_2-NS preparation, the precursor ($(NH_4)_2MoS_4$), bulk MoS_2 and MoS_2-NS were analyzed by XRD and the results were illustrated in Figure 1. As shown in Figure 1, after calcination under N_2, the characteristic peaks of $(NH_4)_2MoS_4$, located at 2θ = 17.2°, 18.44°, and 29.08°, fully vanished, suggesting the evident change of crystal structure. Instead, the peaks at 2θ = 14.6°, 33.48°, 39.82°, and 58.94° were assigned to the (100), (103), (105), and (110) plane of hexagonal MoS_2 phase (JCPDS card No. 65-0160), indicating that after calcination, the obtained bulk MoS_2 was hexagonal phase. The results were similar to Zhang et al.'s findings [24,25]. In addition, after exfoliation by sonication, the resulting MoS_2-NS still kept the same peaks with bulk MoS_2, manifesting that the 2H-MoS_2-NS was successfully obtained. However, compared to the bulk MoS_2, the (002) plane peak of MoS_2-NS became broadened and lower, suggesting an increase of the *d* spacing between MoS_2 layers [26]. Based on the full width at half maximum (FHWM) of the (002) plane, the layer number of the prepared MoS_2-NS could be calculated to be about ~2 layers through Scherrer's equation. To further confirm the structure of the exfoliated MoS_2-NS, Raman spectroscopy (Figure 1b) was employed to characterize the bulk MoS_2 and MoS_2-NS. Both the bulk MoS_2 and MoS_2-NS exhibited two dominant peaks ranging from 340 to 450 cm^{-1}, corresponding to the $E^1{}_{2g}$ and A_{1g} mode of the hexagonal MoS_2, respectively [26,27], which convincingly proved the successful exfoliation of MoS_2-NS. Among which, the $E^1{}_{2g}$ mode peak at 381.6 cm^{-1} involved the in-layer displacements of Mo and S atoms, whereas the A_{1g} mode peak at 407.9 cm^{-1} represented the out-of-layer symmetric displacements of S atoms along the *c*-axis [28]. Noticeably, compared to the bulk MoS_2, the $E^1{}_{2g}$ (377.8 cm^{-1}) and A_{1g} (402.2 cm^{-1}) mode peaks displayed evident blue shift, and the interval (Δ = 24.4 cm^{-1}) between $E^1{}_{2g}$ and A_{1g} peaks was lower than that of bulk MoS_2 (Δ = 26.3 cm^{-1}), which was ascribed to the decrease of the MoS_2 thickness. According to the previous literature [4,25,29], it was found that both $E^1{}_{2g}$ and A_{1g} peaks were the characteristic peaks of MoS_2 and their frequencies would vary with the layer number. When the layer number increases, the interlayer van der Waals force in MoS_2 suppressed atom vibration, resulting in higher force constants [30]. On the contrast, the force constants between the layers would weaken with the layer number decreases. Thus, both $E^1{}_{2g}$ and A_{1g} modes were supposed to stiffen (blue-shift) along with the reduction of MoS_2 layers.

Figure 2a–d presented the FESEM images of the bulk MoS_2 and MoS_2-NS. As seen in Figure 2a,b, the bulk MoS_2 displayed varisized particle-like morphology but clearly thick layer-structure. After exfoliation, the MoS_2-NS exhibited evident thin layer-structure with inconspicuous wrinkle (Figure 2c,d), which suggested the successful exfoliation of MoS_2-NS. Similar to the bulk MoS_2, the size of prepared MoS_2-NS still differed widely. In addition, the thickness of the prepared MoS_2-NS was analyzed by atomic force microscopy (AFM) (Figure 2). As seen in the AFM images (Figure 2e,f), the height profile of the two selected regions displayed a height of ~1.20 nm (±0.03 nm) for MoS_2-NS, which was about 2 times as thick as the theoretical thickness of monolayer MoS_2 (~0.65 nm) [27]. The evident platform of the height curves of the selected MoS_2-NS revealed the smooth surface for MoS_2-NS. Low-resolution TEM image (Figure 2g) also clearly depicted well-stacked layered structures (~2 layers) of the MoS_2-NS, which strongly confirmed the results of XRD and AFM. In the high-resolution TEM (HRTEM) images (Figure 2h), the lattice spacing of 0.27 and 0.16 nm between two adjacent lattice planes could be resolved, which were assigned to the (100) and (110) plane of MoS_2. In addition, the HRTEM image (Figure 2i) and associated fast Fourier transforms (FFT) (Figure 2j) from the center of the MoS_2-NS evidently exhibited hexagonally symmetric structure, which was consistent with the results of XRD analysis. All the above results manifested that the obtained MoS_2-NS still retained hexagonal single crystalline nature during pre-expansion and sonication treatments, which agreed with the previous findings [25,31,32]. However, the BET analysis (Figure 3) showed that the specific

surface areas of bulk MoS_2 and MoS_2-NS were 5.6 and 26.6 m^2 g^{-1}, respectively, indicating that the exfoliation greatly changed the specific surface area of the MoS_2 materials. With the decreasing of the layers, more and more MoS_2 was exposed, resulting in a promotion of the BET surface.

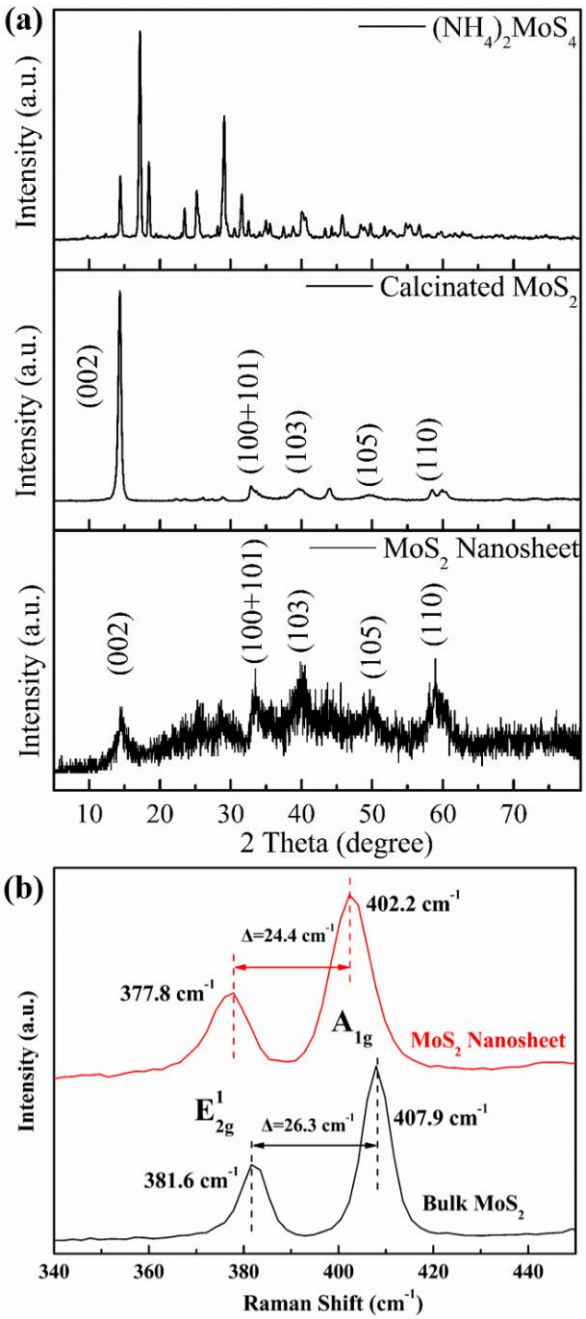

Figure 1. (**a**) XRD patterns of $(NH_4)_2MoS_2$, bulk MoS_2, and MoS_2-NS and (**b**) Raman spectra of bulk MoS_2 and MoS_2 nanosheets.

The chemical composition and element valence on the surface of MoS_2 NS were analyzed with XPS (Figure 4). As depicted in Figure 4a, the survey spectra clearly confirmed the presentence of C, O, NS, and Mo elements. The weak C1s (~284 eV) peak was attributed into the calibration of binding energy with carbon, while the N1s (~400 eV) peak was ascribed into the adsorbed hydrazine hydrate during the sonication. In Mo3d core-level spectra (Figure 4b), the appearance of Mo3d5/2 (233.5 eV) and Mo3d3/2 (232.6 eV) peaks for Mo3d doublet indicated the characteristic +4 oxidation state [1]. Besides, two weak Mo^{6+} 3d peaks (3d5/2 peak at 233.5 eV and 3d3/2 peak at 235.9 eV) were ascribed to

the slight oxidation of MoS_2 NS edge during the MoS_2 transfer under high temperature [25]. In the high-resolution scans of S2p (Figure 4c), two feature peaks (S2p1/2 and S2p3/2) were observed at 162.0 and 163.3 eV, respectively, which greatly matched the binding energy of S^{2-} ions in 2H-MoS_2 [2]. In addition, the appearance of O1s also confirmed the oxidation of MoS_2. In the high-resolution spectra of O1s (Figure 4d), the peak of O^{2-} species located at 532.0 eV and the peak at 533.5 eV was attributed into the absorbed oxygen-containing material like H_2O [3].

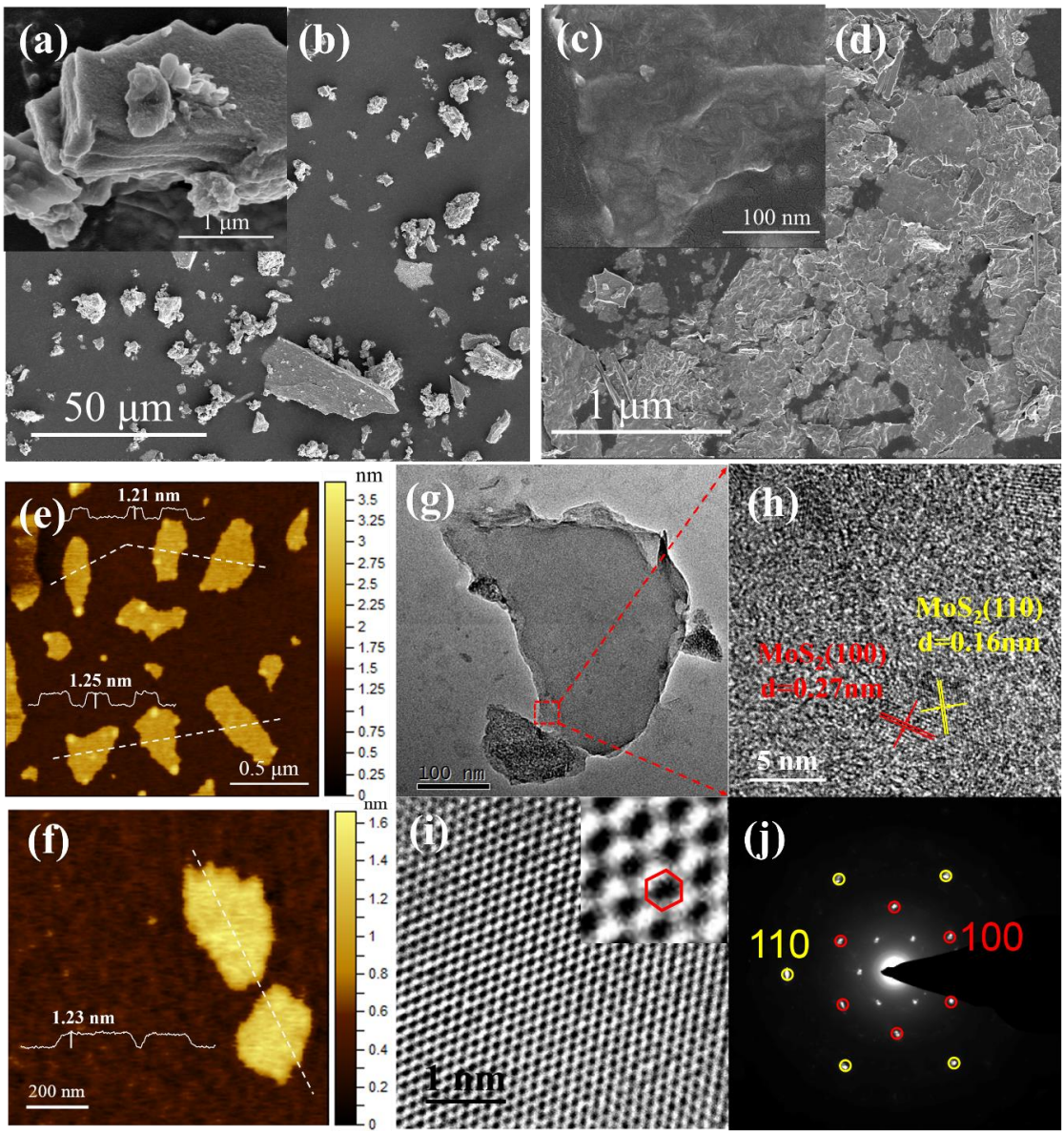

Figure 2. Field emission scanning electron microscope (FESEM) images (**a**–**d**) of the bulk MoS_2 and MoS_2-NS, atomic force microscope (AFM) images (**e**,**f**), height profiles (inset), (transmission electron microscope) TEM and high-resolution transmission electron microscope (HRTEM) images of MoS_2 nanosheets (**g**–**i**), and the fast Fourier transforms (FFT) pattern of MoS_2 NS (**j**).

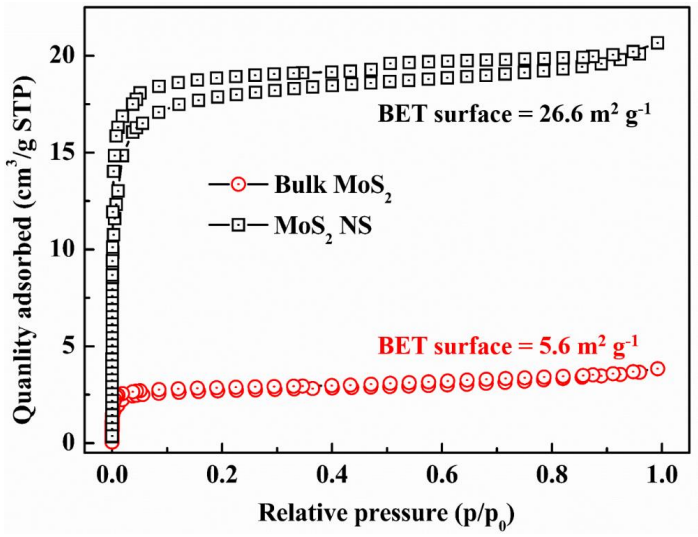

Figure 3. Brunauer–Emmett–Teller (BET) N_2 isotherms of the bulk MoS_2 and MoS_2 NS.

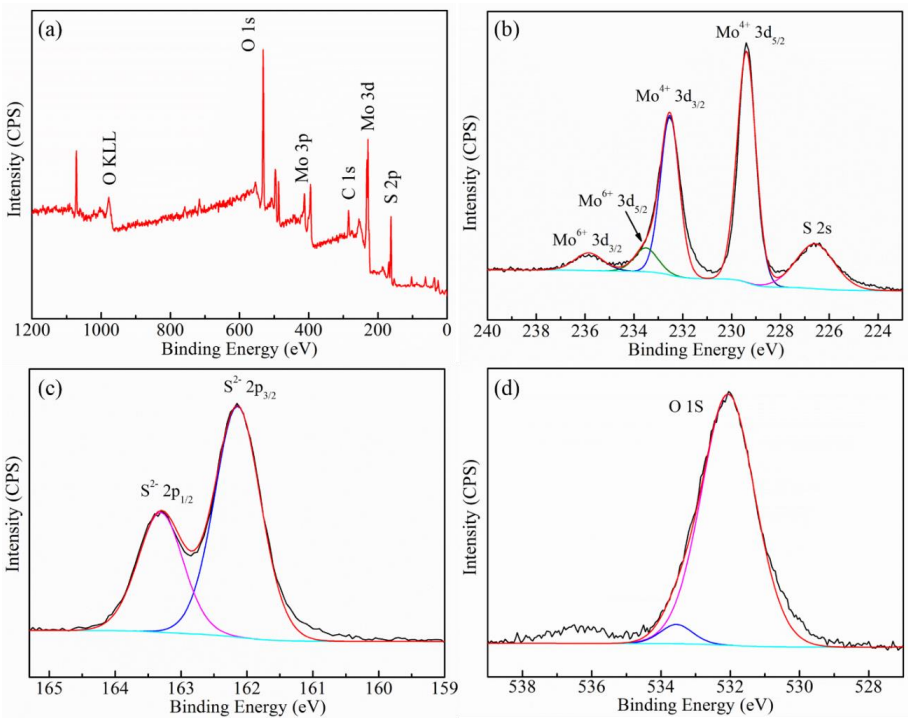

Figure 4. XPS survey spectra of MoS_2 (**a**) and high-resolution scans of Mo3d (**b**), S2p (**c**), O1s (**d**).

3.1.2. Optical Properties of MoS_2 Nanosheets Dispersion

To obtain pure few-layer MoS_2 NS, the suspensions were first centrifuged at 3000 rpm for 2 h to remove the no exfoliated precipitate. Figure 5a displayed the photographs of the as-prepared MoS_2 NS in water. As shown in the Figure 5a, the evident Tyndall phenomenon was observed both of the fresh MoS_2 NS dispersions and the dispersions after 60 days. Meanwhile, the UV-vis absorption spectra (Figure 5b,c) also exhibited no evident change during 60 days. All the results suggested the excellent stability (stable for over 60 days) of as-prepared MoS_2 NS dispersions. In addition, the UV-vis absorption spectra (Figure 5e) of the resulting MoS_2 NS dispersions with different concentrations (Figure 5d) displayed two distinctly characteristic peaks for 2H-MoS_2 [33]. The two peaks located at 615 (B-exciton) and 670 nm (A-exciton) were attributed to the direct excitonic transitions of MoS_2 at the

K point of the Brillouin zone [34,35]. According to Hai et al.'s study [25], the relationship between the concentrations of MoS_2 NS dispersions and the measured absorbance at a given wavelength (615 or 670 nm) were estimated by using the Beer–Lambert law. The fitting results (Figure 5f) proved that the concentrations of the dispersions showed good linear relationship (R^2 = 0.9996) with the absorbance at 615 nm in the range of 0.01–0.5 mg L^{-1}, which meant that the quantitative analysis of the MoS_2 NS dispersions was available. Based on the above relationship, the concentration of the as-prepared MoS_2 NS dispersions was 0.65 ± 0.04 mg mL^{-1}, which was much higher than previous findings [7,25]. The initial concentration of the bulk MoS_2 (2.510 g of bulk MoS_2 were obtained after the calcination of $(NH_4)_2MoS_4$) was 2.51 mg mL^{-1}, and the corresponding few-layer MoS_2 NS yield was calculated to be as high as 25.9% in water.

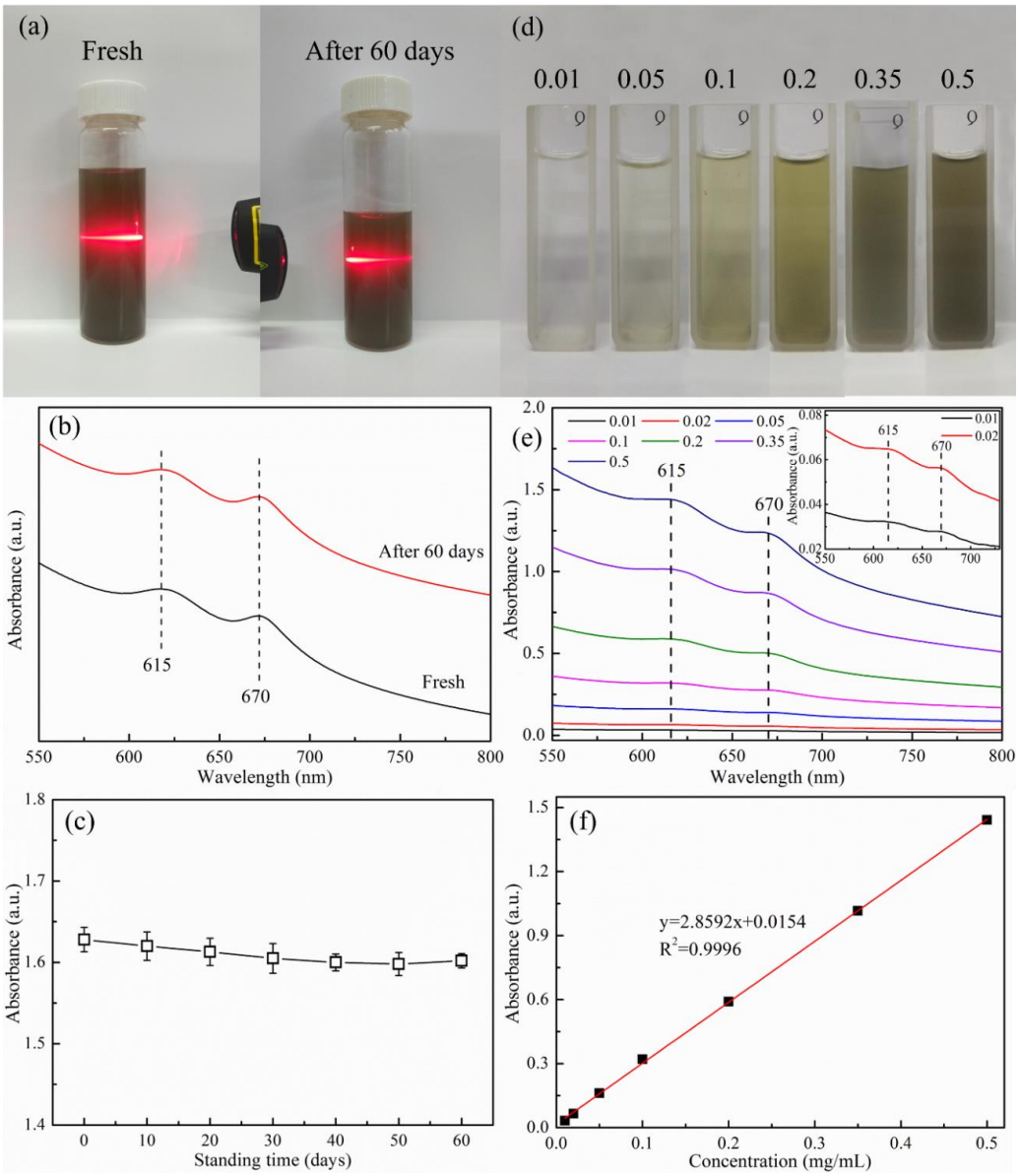

Figure 5. Photographs (**a**), UV-vis absorption spectra (**b**), absorbance change with standing time (**c**) of the prepared MoS_2 NS dispersions and photographs (**d**), UV-vis absorption spectra (**e**) and standard curve (**f**) of MoS_2 NS dispersion in different concentrations.

3.2. *Adsorption Behavior of MoS_2-NS Towards Dyes and Heavy Metals*

3.2.1. Adsorption Isotherms and Kinetics

The adsorption performance of the MoS_2 NS was tested by selecting two dyes (methylene blue, MB and methyl orange, MO) and three heavy metal ions (Cu^{2+}, Cd^{2+}, and Ag^{+}) as the targets. As seen in Figure 6a, in the bulk MoS_2 systems, the equilibrium adsorption capacities of the two dyes only slightly increased with the increasing of the dye concentrations, manifesting that the bulk MoS_2 exhibited unsatisfactory adsorption performance of MB and MO. Instead, the equilibrium adsorption capacities of MoS_2 NS for MB and MO significantly increased under high concentration of dyes, which were much larger than those of bulk MoS_2. Meanwhile, the as-prepared MoS_2 NS also displayed more excellent adsorption performance on heavy metals than the bulk MoS_2. All the results indicated that the exfoliation was beneficial to improve the adsorption performance of MoS_2, which was in accordance with previous studies [3,36,37].

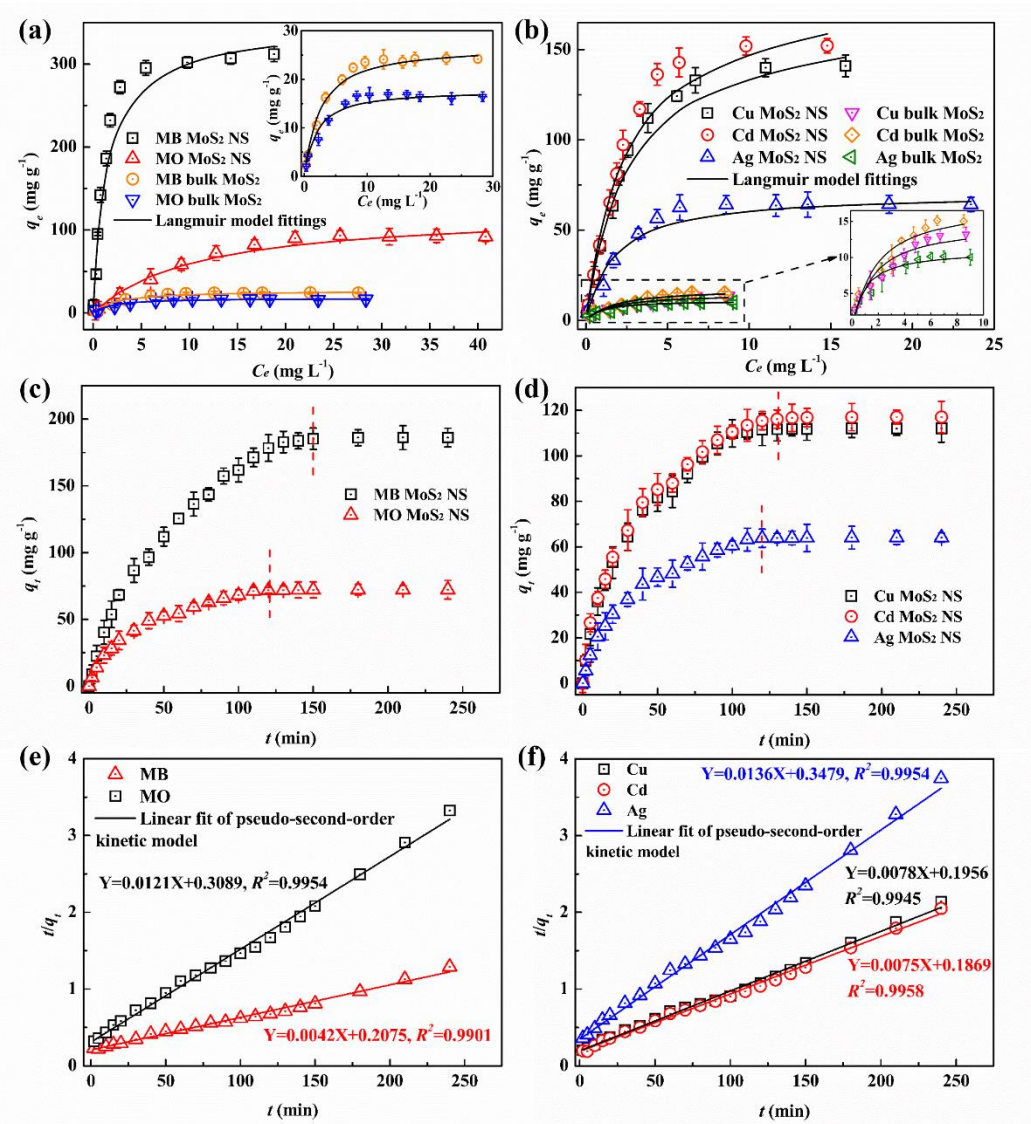

Figure 6. Adsorption isotherms (**a**) and kinetics (**c**,**e**) of MB, MO for bulk MoS_2 and MoS_2 NS at 20 mg L^{-1}; adsorption isotherms (**b**) and kinetics (**d**,**f**) of Cu^{2+}, Cd^{2+} and Ag^{+} for bulk MoS_2 and MoS_2 NS at 15 mg L^{-1}.

In addition, to well study the adsorption behavior, the Langmuir and Freundlich models were employed to fit the experimental data (Figure 6a,b, Figure S1). As listed in Table 1, the high R^2 values suggested that the Langmuir model better described the adsorption of dyes and heavy metals onto MoS_2 NS and bulk MoS_2 than the Freundlich model. Based on the Langmuir model fitting, the relative parameters like the maximum adsorption capacity (q_m) and affinity constant (K_L) for dyes and heavy metals were obtained and listed in Table 1. The q_m values of MB and MO for MoS_2 NS were 344.8 and 123.5 mg g^{-1}, respectively, which were 12.77 and 6.94 larger than those (27.0 and 17.8 mg g^{-1} for MB and MO, respectively) of bulk MoS_2. Meanwhile, the similar results were observed in the heavy metal adsorption, indicating that the MoS_2 NS exhibited much more excellent adsorption performance than the bulk MoS_2. In addition, for the dyes, the higher q_m and K_L values of MB implied that MoS_2 materials exhibited better adsorption capacity and affinity to MB. For heavy metals, the highest q_m value occurred to Cd^{2+} (185.2 mg g^{-1}), following Cu^{2+} (169.5 mg g^{-1}) and Ag^+ (70.4 mg g^{-1}), indicating that MoS_2 NS were more beneficial to Cd^{2+} and Cu^{2+} adsorption than Ag^+.

Table 1. Fitted parameters for the adsorption of dyes and heavy metals on MoS_2 NS and bulk MoS_2.

Samples	Targets	Langmuir Model			Freundlich Model		
		q_m (mg g^{-1})	K_L (L mg^{-1})	R^2	$1/n$	K_f (L g^{-1})	R^2
MoS_2 NS	MB	344.8	0.725	0.994	0.648	92.796	0.875
	MO	123.5	0.393	0.980	0.724	9.023	0.969
Bulk MoS_2	MB	27.0	0.238	0.996	0.504	6.381	0.915
	MO	17.8	0.187	0.992	0.449	4.988	0.904
MoS_2 NS	Cd^{2+}	185.2	0.606	0.985	0.708	40.496	0.943
	Cu^{2+}	169.5	0.588	0.989	0.693	35.848	0.938
	Ag^+	70.4	0.339	0.993	0.533	18.326	0.914
Bulk MoS_2	Cd^{2+}	18.7	0.297	0.952	0.463	6.069	0.979
	Cu^{2+}	16.3	0.285	0.963	0.459	5.321	0.991
	Ag^+	11.7	0.134	0.987	0.389	4.913	0.968

Figure 6c,d displayed adsorption kinetics data for dyes and heavy metals over MoS_2 NS. As revealed in Figure 6c, both MO and MB adsorption increased rapidly at the beginning, then proceeded at a slower rate, and tended to equilibrium at the end. The similar results occurred to the adsorption of heavy metals. Besides, to further analyze the time-dependent variation during the adsorption process, pseudo-first-order and pseudo-second-order kinetic models were employed to fit the dyes and heavy metals adsorption on MoS_2 NS (Figure 6e,f). As shown in Table S1, the higher R^2 values suggested that the pseudo-second-order model better described both dyes and heavy metals adsorption than the pseudo-first-order model, suggesting that the electron transfer between MoS_2 NS and dye molecule or metal ions played a controlling role during the adsorption [38].

3.2.2. Adsorption Mechanism

Based on the results, the MoS_2 NS showed much better dye or metal adsorption performance than bulk MoS_2. According to the previous studies [3,37,39,40], the main mechanisms reported during the adsorption of dyes or metal by the inorganic materials involved physical hole-filling effects, electrostatic interactions, and ion exchange.

Physical Hole-Filling Effects

The specific surface area often displayed significant effect on the adsorption of the pollutants [41–43]. The adsorbents with large specific surface area usually owned abundant pores, which greatly provided a sufficient adsorption site to capture the pollutants, resulting in the promotion of their adsorption performance. For nano materials, the physical hole-filling effect was considered as one of the important

adsorption mechanisms [41]. According to above-mentioned results, the obtained MoS_2 NS owned much larger specific surface area than bulk MoS_2, while the MoS_2 NS also exhibited more excellent adsorption performance on dyes and heavy metals. Thus, it could be inferred that the physical hole-filling effect probably played a vital role in the promotion of dyes or heavy metal adsorption. Herein, to verify the role of specific surface area during the dyes or heavy metal adsorption over MoS_2 NS and bulk MoS_2, the obtained q_e data were standardized with the BET surface area and the results were showed in Figure 7. As shown in Figure 7a, for dyes, the equilibrium adsorption capacities of MoS_2 NS for MB and MO were 312.0 and 92.6 mg g^{-1}, which were 12.89 and 5.61 times larger than those of bulk MoS_2, respectively. Meanwhile, the as-prepared MoS_2 NS also displayed excellent adsorption performance on heavy metals (Figure 7c), with 141.0, 152.8, and 64.2 mg g^{-1} for Cu^{2+}, Cd^{2+}, and Ag^{+}, respectively, which were 10.68, 10.12, and 6.42 folds larger than those of bulk MoS_2 (13.2, 15.1, and 10.0 mg g^{-1} for Cu^{2+}, Cd^{2+}, and Ag^{+}, respectively). After standardization (Figure 7b,d), all of the q_e ratios between the MoS_2 NS and bulk MoS_2 significantly decreased from 12.89 (MB), 5.61 (MO), 10.12 (Cu^{2+}), 10.68 (Cd^{2+}), and 6.42 (Ag^{+}) to 2.72, 1.12, 2.24, 2.11, and 1.33, respectively, suggesting that the physical hole-filling effect played positive role in the promotion of dyes or heavy metal adsorption over MoS_2.

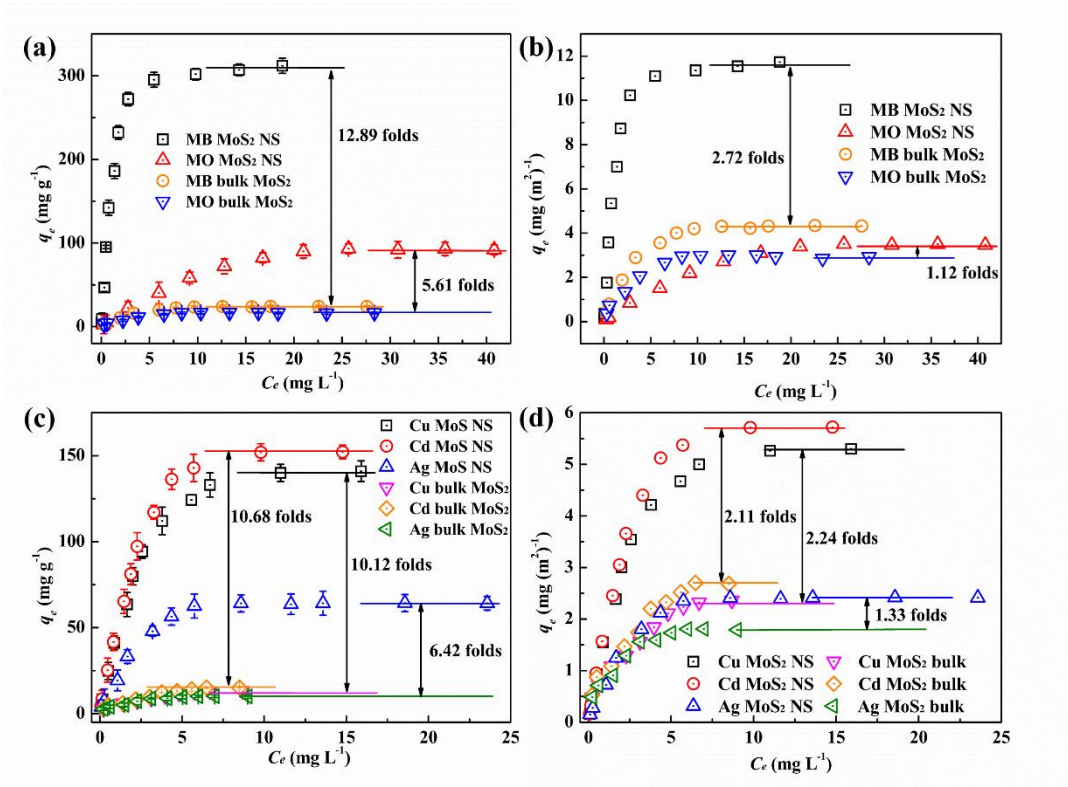

Figure 7. Equilibrium adsorption capacity (**a**,**c**) and standardized equilibrium adsorption capacity (**b**,**d**) of dyes (MO and MB) and heavy metals (Cu^{2+}, Cd^{2+}, and Ag^{+}) for bulk MoS_2 and MoS_2 NS.

In addition, no evident variation was observed between the standardized q_e values of MoS_2 NS and bulk MoS_2 (Figure 7b), meaning that the physical hole-filling effect was the sole mechanism during MO adsorption over MoS_2 NS. However, the significant enhancement between the standardized q_e values of MoS_2 NS and bulk MoS_2 (Figure 7b,d) suggested that besides the physical hole-filling effect, some other mechanisms were involved during the adsorption of MB and heavy metals over MoS_2 NS.

Electrostatic Interactions

Electrostatic interaction was often considered as a possible mechanism to explain the adsorption of dyes and heavy metals [37,40,44]. To confirm the role of electrostatic interaction during dyes and

heavy metals adsorption over MoS_2 NS, the adsorption efficiency in various pH values were conducted. As depicted in Figure 8a, the slight fluctuation among the q_e values for MO suggested that the MB adsorption over MoS_2 NS was not controlled by the pH values. Instead, the MB adsorption was notably influenced by the pH values. At low pH (<6) conditions, the q_e values increased with the pH value and reached a peak (186.2 mg g^{-1}) at pH = 6.0, and then gradually declined when pH > 6. Meanwhile, Zeta potential results (Figure 8c) showed that the isoelectric point of MoS_2 NS was about 3.8. This meant that the surface of MoS_2 NS displayed a positive charge when the pH value was below 3.8, while a negative charge above 3.8. As a typical cationic dye, MB molecules could strongly adhere to the MoS_2 NS through the electrostatic interaction once the surface charge of MoS_2 NS turned to negative, leading to an increasing of the q_e values.

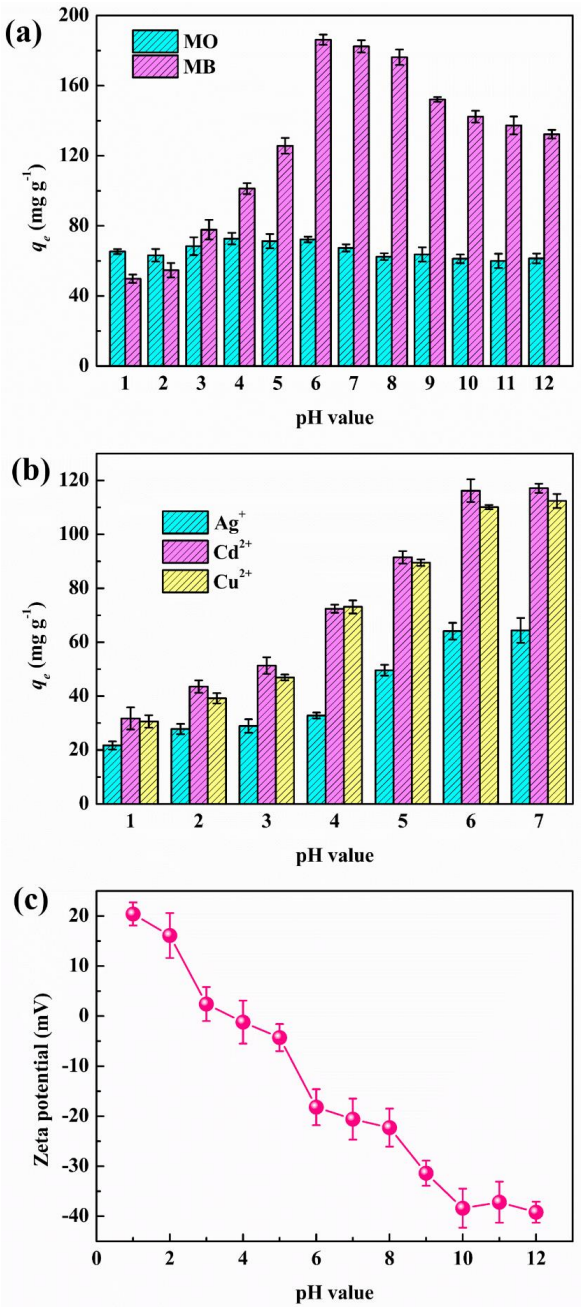

Figure 8. Effects of pH on dyes (**a**) and heavy metals (**b**) over MoS_2 NS, and the Zeta potential (**c**) of MoS_2 NS at different pH values. For dyes: 20 mg L^{-1} of the initial concentration, for heavy metals: 15 mg L^{-1} of the initial concentration.

Similarly, the pH also markedly influenced the adsorption of heavy metals over MoS_2 NS (Figure 8b). The q_e values of Cu^{2+}, Cd^{2+}, and Ag^+ evidently increased with an increasing pH, and stabilized at about 112.4, 117.0, and 64.4 mg g^{-1}, respectively. When the pH increased, the surface charge of MoS_2 NS turned to negative and the values gradually increased, which meant that stronger electrostatic interaction occurred between the heavy metal ions and MoS_2 NS at higher pH, resulting in improvement of the adsorption performance. In addition, the charge values of the heavy metal ions also showed visible effects on the adsorption capacity. Due to the lower value of the charge for Ag^+, the q_e value of Ag^+ was much lower than those of Cu^{2+} and Cd^{2+}, which was ascribed into the weaker electrostatic interaction between Ag^+ and MoS_2 NS. According to the Coulomb law, electrostatic interaction was in direct proportion to the value of the surface charge. The similar results were also found in Yang at al.'s studies [45].

Ion Exchange

According to previous studies [43,46], the ion exchange only occurred with heavy metals adsorption. It was well known that the affinity to the metal ions in the ion exchange process increased with the ion radius and the ion radius of Cd^{2+} and Cu^{2+} were 0.97 Å and 0.73 Å, respectively. If the ion exchange was the main adsorption mechanism, the number of the adsorbed Cd^{2+} should be larger than that of Cu^{2+}. Actually, in the system of 15 mg^{-1} L (Figure 8b), the molar adsorption capacity of Cd^{2+} (1.04 mmol g^{-1}, 117.0 mg g^{-1}) was visibly lower than that of Cu^{2+} (1.75 mmol g^{-1},112.4 mg g^{-1}), which indicated that the ion exchange was not the main mechanism during the heavy metals over MoS_2 NS. Similarly, Nguyen et al. also found that the ion exchange played a negligible role during the Cd^{2+} and Cu^{2+} adsorption over the activated carbon [43].

4. Conclusions

In summary, the ultrathin 2H-MoS_2 nanosheets with 1–2 layers were successfully obtained via a hybrid stagey with combination of quenching process and liquid-based exfoliation. The as-prepared 2H-MoS_2 nanosheets exhibited evident optical properties and could be accurately quantified with the absorbance at 615 nm in the range of 0.01–0.5 mg L^{-1}. Besides, the obtained 2H-MoS_2 nanosheets also showed a promising application in pollution control. It could be a candidate absorbent for the removal of dyes and heavy metals. This work provided an effective way for the large-scale fabrication of the two-dimensional nanosheets of transition metal dichalcogenides (TMDs) by liquid exfoliation.

Supplementary Materials: The following are available online at http://www.mdpi.com/2227-9717/8/5/504/s1, Figure S1. Linear fittings of dyes adsorption (a) and heavy metals (b and c) over bulk MoS2 and MoS2 NS with the Freundlich model, Table S1 Adsorption kinetics parameters of dyes and heavy metals adsorption over MoS2 NS.

Author Contributions: S.H. and Y.L. (Yifan Liu) conceived the study, designed the experiments and wrote the manuscript. S.H., Z.Y. and Y.J. performed the experiments. F.Z. and K.L. finished the characterization and data analysis. Y.L. (Yuancai Lv) and X.C. edited the manuscript. All authors have read and agreed to the published version of the manuscript.

Funding: This research was funded by by the Open Project Program of National Engineering Research Center for Environmental Photocatalysis (Grant No. 201904), Fuzhou University.

Conflicts of Interest: The authors declare no conflict of interest.

References

1. Kibsgaard, J.; Chen, Z.; Reinecke, B.N.; Jaramillo, T.F. Engineering the surface structure of MoS_2 to preferentially expose active edge sites for electrocatalysis. *Nat. Mater.* **2012**, *11*, 963–969. [CrossRef] [PubMed]
2. Oakes, L.; Carter, R.; Hanken, T.; Cohn, A.P.; Share, K.; Schmidt, B.; Pint, C.L. Interface strain in vertically stacked two-dimensional heterostructured carbon-MoS_2 nanosheets controls electrochemical reactivity. *Nat. Commun.* **2016**, *7*, 11796. [CrossRef] [PubMed]

3. Qiao, X.-Q.; Tian, F.-Y.; Hou, D.-F.; Hu, F.-C.; Li, D.-S. Equilibrium and kinetic studies on MB adsorption by ultrathin 2D MoS_2 nanosheets. *RSC Adv.* **2016**, *6*, 11631–11636. [CrossRef]
4. Ye, L.; Xu, H.; Zhang, D.; Chen, S. Synthesis of bilayer MoS_2 nanosheets by a facile hydrothermal method and their methyl orange adsorption capacity. *Mater. Res. Bull.* **2014**, *55*, 221–228. [CrossRef]
5. Lee, C.; Yan, H.; Brus, L.E.; Heinz, T.F.; Hone, J.; Ryu, S. Anomalous Lattice Vibrations of Single- and Few-Layer MoS_2. *ACS Nano* **2010**, *4*, 2695–2700. [CrossRef] [PubMed]
6. Zhang, Y.; Ye, J.; Matsuhashi, Y.; Iwasa, Y. Ambipolar MoS_2 Thin Flake Transistors. *Nano Lett.* **2012**, *12*, 1136–1140. [CrossRef]
7. Coleman, J.N.; Lotya, M.; O'Neill, A.; Bergin, S.D.; King, P.J.; Khan, U.; Young, K.; Gaucher, A.; De, S.; Smith, R.J.; et al. Two-Dimensional Nanosheets Produced by Liquid Exfoliation of Layered Materials. *Science* **2011**, *331*, 568–571. [CrossRef]
8. O'Neill, A.; Khan, U.; Coleman, J.N. Preparation of High Concentration Dispersions of Exfoliated MoS_2 with Increased Flake Size. *Chem. Mater.* **2012**, *24*, 2414–2421. [CrossRef]
9. Tao, J.; Chai, J.W.; Lü, X.; Wong, L.M.; Wong, T.I.; Pan, J.; Xiong, Q.; Chi, D.; Wang, S. Growth of wafer-scale MoS_2 monolayer by magnetron sputtering. *Nanoscale* **2015**, *7*, 2497–2503. [CrossRef]
10. Motola, M.; Baudys, M.; Zazpe, R.; Krbal, M.; Michalicka, J.; Rodriguez-Pereira, J.; Pavlinak, D.; Prikryl, J.; Hromadko, L.; Sopha, H.I.; et al. 2D MoS2 nanosheets on 1D anodic TiO_2 nanotube layers: An efficient co-catalyst for liquid and gas phase photocatalysis. *Nanoscale* **2019**, *11*, 23126–23131. [CrossRef] [PubMed]
11. Shen, J.; He, Y.; Wu, J.; Gao, C.; Keyshar, K.; Zhang, X.; Yang, Y.; Ye, M.; Vajtai, R.; Lou, J.; et al. Liquid Phase Exfoliation of Two-Dimensional Materials by Directly Probing and Matching Surface Tension Components. *Nano Lett.* **2015**, *15*, 5449–5454. [CrossRef] [PubMed]
12. Kim, J.; Kwon, S.; Cho, D.-H.; Kang, B.; Kwon, H.; Kim, Y.; Park, S.O.; Jung, G.Y.; Shin, E.; Kim, W.-G.; et al. Direct exfoliation and dispersion of two-dimensional materials in pure water via temperature control. *Nat. Commun.* **2015**, *6*, 8294. [CrossRef] [PubMed]
13. Dong, L.; Lin, S.; Yang, L.; Zhang, J.; Yang, C.; Yang, D.; Lu, H. Spontaneous exfoliation and tailoring of MoS_2 in mixed solvents. *Chem. Commun.* **2014**, *50*, 15936–15939. [CrossRef] [PubMed]
14. Zhou, K.-G.; Mao, N.-N.; Wang, H.; Peng, Y.; Zhang, H.-L. A Mixed-Solvent Strategy for Efficient Exfoliation of Inorganic Graphene Analogues. *Angew. Chem. Int. Ed.* **2011**, *50*, 10839–10842. [CrossRef] [PubMed]
15. Guardia, L.; Paredes, J.I.; Rozada, R.; Villar-Rodil, S.; Martinez-Alonso, A.; Tascón, J.D. Production of aqueous dispersions of inorganic graphene analogues by exfoliation and stabilization with non-ionic surfactants. *RSC Adv.* **2014**, *4*, 14115–14127. [CrossRef]
16. Smith, R.J.; King, P.J.; Lotya, M.; Wirtz, C.; Khan, U.; De, S.; O'Neill, A.; Duesberg, G.S.; Grunlan, J.C.; Moriarty, G.; et al. Large-Scale Exfoliation of Inorganic Layered Compounds in Aqueous Surfactant Solutions. *Adv. Mater.* **2011**, *23*, 3944–3948. [CrossRef]
17. Zheng, J.; Zhang, H.; Dong, S.; Liu, Y.; Nai, C.T.; Shin, H.S.; Jeong, H.Y.; Liu, B.; Loh, K.P. High yield exfoliation of two-dimensional chalcogenides using sodium naphthalenide. *Nat. Commun.* **2014**, *5*, 2995. [CrossRef]
18. Zhuc, W.; Gao, X.; Li, Q.; Li, H.; Chao, Y.; Li, M.; Mahurin, S.M.; Li, H.; Zhu, H.; Dai, S. Controlled Gas Exfoliation of Boron Nitride into Few-Layered Nanosheets. *Angew. Chem. Int. Ed.* **2016**, *55*, 10766–10770. [CrossRef]
19. Jiang, B.; Tian, C.; Wang, L.; Xu, Y.; Wang, R.; Qiao, Y.; Ma, Y.; Fu, H. Facile fabrication of high quality graphene from expandable graphite: Simultaneous exfoliation and reduction. *Chem. Commun.* **2010**, *46*, 4920. [CrossRef]
20. Tang, Y.B.; Lee, C.-S.; Chen, Z.; Yuan, G.D.; Kang, Z.H.; Luo, L.B.; Song, H.S.; Liu, Y.; He, Z.; Zhang, W.; et al. High-Quality Graphenes via a Facile Quenching Method for Field-Effect Transistors. *Nano Lett.* **2009**, *9*, 1374–1377. [CrossRef]
21. Van Thanh, D.; Pan, C.-C.; Chu, C.-W.; Wei, K.-H. Production of few-layer MoS2nanosheets through exfoliation of liquid N2–quenched bulk MoS_2. *RSC Adv.* **2014**, *4*, 15586–15589. [CrossRef]
22. Zhao, J.; Wang, Z.; Zhao, Q.; Xing, B. Adsorption of Phenanthrene on Multilayer Graphene as Affected by Surfactant and Exfoliation. *Environ. Sci. Technol.* **2013**, *48*, 331–339. [CrossRef] [PubMed]
23. Cao, Q.; Huang, F.; Zhuang, Z.; Lin, Z. A study of the potential application of nano-$Mg(OH)_2$ in adsorbing low concentrations of uranyl tricarbonate from water. *Nanoscale* **2012**, *4*, 2423. [CrossRef] [PubMed]

24. Zhang, D.-Q.; Chai, J.-X.; Jia, Y.-X.; Wang, L.-J.; Zhao, Z.-L.; Cao, M. Facile Preparation of Few-layer MoS_2-NS by Liquid-Phase Ultrasonic Exfoliation. In Proceedings of the 2017 International Conference on Manufacturing Engineering and Intelligent Materials (ICMEIM 2017), Guangzhou, China, 25–26 February 2017.
25. Hai, X.; Chang, K.; Pang, H.; Li, M.; Li, P.; Liu, H.; Shi, L.; Ye, J. Engineering the Edges of MoS_2 (WS_2) Crystals for Direct Exfoliation into Monolayers in Polar Micromolecular Solvents. *J. Am. Chem. Soc.* **2016**, *138*, 14962–14969. [CrossRef]
26. Ma, L.; Huang, G.; Chen, W.; Wang, Z.; Ye, J.; Li, H.; Chen, D.; Lee, J.Y. Cationic surfactant-assisted hydrothermal synthesis of few-layer molybdenum disulfide/graphene composites: Microstructure and electrochemical lithium storage. *J. Power Sources* **2014**, *264*, 262–271. [CrossRef]
27. Li, H.; Zhang, Q.; Yap, C.C.R.; Tay, B.K.; Edwin, T.H.T.; Olivier, A.; Baillargeat, D. From Bulk to Monolayer MoS_2: Evolution of Raman Scattering. *Adv. Funct. Mater.* **2012**, *22*, 1385–1390. [CrossRef]
28. Korn, T.; Heydrich, S.; Hirmer, M.; Schmutzler, J.; Schüller, C. Low-temperature photocarrier dynamics in monolayer MoS_2. *Appl. Phys. Lett.* **2011**, *99*, 102109. [CrossRef]
29. Chakraborty, B.; Matte, H.R.; Sood, A.K.; Ra, C.N.R. Layer-dependent resonant Raman scattering of a few layer MoS_2. *J. Raman Spectrosc.* **2013**, *44*, 92–96. [CrossRef]
30. Bagnall, A.; Liang, W.; Marseglia, E.; Welber, B. Raman studies of MoS_2 at high pressure. *Phys. B+C* **1980**, *99*, 343–346. [CrossRef]
31. Chou, S.S.; De, I.; Kim, J.; Byun, S.; Dykstra, C.; Yu, J.; Huang, J.; Dravid, V.P. Ligand Conjugation of Chemically Exfoliated MoS_2. *J. Am. Chem. Soc.* **2013**, *135*, 4584–4587. [CrossRef]
32. Wang, L.; Xu, Z.; Wang, W.; Bai, X. Atomic Mechanism of Dynamic Electrochemical Lithiation Processes of MoS_2 Nanosheets. *J. Am. Chem. Soc.* **2014**, *136*, 6693–6697. [CrossRef]
33. Wilcoxon, J.P.; Newcomer, P.P.; Samara, G.A. Synthesis and optical properties of MoS_2 and isomorphous nanoclusters in the quantum confinement regime. *J. Appl. Phys.* **1997**, *81*, 7934–7944. [CrossRef]
34. Guan, G.; Zhang, S.; Liu, S.; Cai, Y.; Low, M.; Teng, C.P.; Phang, I.Y.; Cheng, Y.; Duei, K.L.; Srinivasan, B.M.; et al. Protein Induces Layer-by-Layer Exfoliation of Transition Metal Dichalcogenides. *J. Am. Chem. Soc.* **2015**, *137*, 6152–6155. [CrossRef] [PubMed]
35. Mak, K.F.; Lee, C.; Hone, J.; Shan, J.; Heinz, T.F. Atomically Thin MoS_2: A New Direct-Gap Semiconductor. *Phys. Rev. Lett.* **2010**, *105*, 1–4. [CrossRef] [PubMed]
36. Wu, P.; Yin, N.; Li, P.; Cheng, W.; Huang, M. The adsorption and diffusion behavior of noble metal adatoms (Pd, Pt, Cu, Ag and Au) on a MoS_2 monolayer: A first-principles study. *Phys. Chem. Chem. Phys.* **2017**, *19*, 20713–20722. [CrossRef]
37. Zhan, W.; Jia, F.; Yuan, Y.; Liu, C.; Sun, K.; Yang, B.; Song, S. Controllable incorporation of oxygen in MoS_2 for efficient adsorption of Hg^{2+} in aqueous solutions. *J. Hazard. Mater.* **2020**, *384*, 121382. [CrossRef]
38. Lv, Y.; Zhang, R.; Zeng, S.; Liu, K.; Huang, S.; Liu, Y.; Xu, P.; Lin, C.; Cheng, Y.; Liu, M. Removal of p-arsanilic acid by an amino-functionalized indium-based metal–organic framework: Adsorption behavior and synergetic mechanism. *Chem. Eng. J.* **2018**, *339*, 359–368. [CrossRef]
39. Yang, H.; Yuan, H.; Hu, Q.; Liu, W.; Zhang, D. Synthesis of mesoporous C/MoS2 for adsorption of methyl orange and photo-catalytic sterilization. *Appl. Surf. Sci.* **2020**, *504*, 144445. [CrossRef]
40. Luo, J.; Fu, K.; Sun, M.; Yin, K.; Wang, D.; Liu, X.; Crittenden, J.C. Phase-Mediated Heavy Metal Adsorption from Aqueous Solutions Using Two-Dimensional Layered MoS_2. *ACS Appl. Mater. Interfaces* **2019**, *11*, 38789–38797. [CrossRef]
41. Choi, M.; Jang, J. Heavy metal ion adsorption onto polypyrrole-impregnated porous carbon. *J. Colloid Interface Sci.* **2008**, *325*, 287–289. [CrossRef]
42. Li, H.; Xie, F.; Li, W.; Fahlman, B.D.; Chen, M.; Li, W. Preparation and adsorption capacity of porous MoS_2 nanosheets. *RSC Adv.* **2016**, *6*, 105222–105230. [CrossRef]
43. Nguyen, H.D.; Tran, H.N.; Chao, H.-P.; Lin, C.-C. Activated Carbons Derived from Teak Sawdust-Hydrochars for Efficient Removal of Methylene Blue, Copper, and Cadmium from Aqueous Solution. *Water* **2019**, *11*, 2581. [CrossRef]

44. Li, R.; Deng, H.; Zhang, X.; Wang, J.J.; Awasthi, M.K.; Wang, Q.; Xiao, R.; Zhou, B.; Du, J.; Zhang, Z. High-efficiency removal of Pb(II) and humate by a CeO_2–MoS_2 hybrid magnetic biochar. *Bioresour. Technol.* **2019**, *273*, 335–340. [CrossRef] [PubMed]
45. Yang, K.; Chen, B.; Zhu, X.; Xing, B. Aggregation, Adsorption, and Morphological Transformation of Graphene Oxide in Aqueous Solutions Containing Different Metal Cations. *Environ. Sci. Technol.* **2016**, *50*, 11066–11075. [CrossRef] [PubMed]
46. Wang, C.; Yang, R.; Wang, H. Synthesis of ZIF-8/Fly Ash Composite for Adsorption of Cu^{2+}, Zn^{2+} and Ni^{2+} from Aqueous Solutions. *Materials* **2020**, *13*, 214. [CrossRef] [PubMed]